GDCh Research Article Angewandte International Edition Chemie www.angewandte.org

How to cite: *Angew. Chem. Int. Ed.* **2025**, *64*, e202507352
doi.org/10.1002/anie.202507352

Aqueous Zn-Ion Batteries

Ni-Bis(dithiolene) Coordination Enhanced Dual-Functional Covalent Organic Frameworks for both Cathodic Zn^{2+} Storage and Anodic Zinc Deposition Control in Aqueous Zn-Ion Batteries

Qianchuan Yu[+], Tianyu Shen[+], Si-Wen Ke[+], Kaiqiang Zhang, Xinmei Song, Jingjie Sun, Zuoao Wu, Miao Wang, Yongxin Yang, Zedong Zhang, Anqi Zhang, Zuoxiu Tie, Yichao Yan,* Jing Ma,* Jinglin Zuo,* and Zhong Jin**

Abstract: In response to the increasing demand for sustainable energy storage solutions, aqueous zinc-ion batteries (AZIBs) have garnered significant attention for their high safety, low cost, and environmental friendliness. However, two major challenges to battery stability persist: developing efficient cathode materials and addressing zinc dendrite formation. Here, we report a dual-functional covalent organic framework (COF), named Ni–DAPTO, designed to improve both Zn^{2+} storage on the cathode and zinc deposition kinetics on the anode. The incorporation of Ni coordination centers achieves an expected low energy gap, enhancing the intrinsic conductivity, while selectively guiding uniform Zn^{2+} deposition. As a result, the Ni–DAPTO cathode demonstrated superior cycling stability and rate performance, retaining a specific capacity of 127.0 and 119.7 mAh g^{-1} at 0.5 and 10.0 A g^{-1}, respectively after 10 000 cycles. Besides, when employed as artificial solid electrolyte interphase (SEI), Ni–DAPTO can improve zinc utilization and inhibit dendrite formation. The full AZIBs assembled with Ni–DAPTO cathodes and Ni–DAPTO modified Zn anodes deliver a discharge capacity of 100.9 mAh g^{-1} after 1000 cycles at a current density of 5.0 A g^{-1}. These findings suggest that multifunctional COFs hold great potential for advancing high-performance and long-lasting aqueous secondary batteries.

Introduction

With the rising global demand for sustainable energy solutions, the development of efficient and reliable energy storage systems has become a critical focus in the pursuit of carbon neutrality.[1–4] Among various energy storage technologies, aqueous zinc-ion batteries (AZIBs) have emerged as a promising alternative to traditional lithium-ion batteries due to their inherent advantages, including high safety, low cost, and environmental friendliness.[5–7] Unlike lithium-ion systems, AZIBs operate in non-flammable aqueous electrolytes, reducing safety risks, while zinc, as an anode material, offers high theoretical capacity (820 mAh g^{-1}), abundant natural reserves, and low environmental impact.[8–10] Despite these advantages, the widespread application of AZIBs is hindered by two significant challenges: the development of advanced cathode materials with high energy efficiency and long cycle life, and the suppression of zinc dendrite formation during repeated charge/discharge cycles.

On the cathode side, organic materials have garnered interest due to their structural diversity, lightweight nature, and tunability.[11–15] Notably, organic molecules containing highly conjugated functional groups such as C=O and C=N have been proven effective in reversibly capturing-releasing Zn^{2+} ions via redox reactions, thus contributing significant specific capacities.[16–19] However, the inherent solubility and low conductivity of organic cathodes lead to issues such as capacity fading, poor cycling stability, inferior rate performance, and slow kinetics, impeding the practical use of organic cathodes in AZIBs.[20–23] Simultaneously,

[*] Q. Yu[+], Dr. T. Shen[+], Dr. S.-W. Ke[+], Dr. K. Zhang, Dr. X. Song, J. Sun, Z. Wu, Dr. M. Wang, Y. Yang, Z. Zhang, A. Zhang, Dr. Z. Tie, Prof. Y. Yan, Prof. J. Ma, Prof. J. Zuo, Prof. Z. Jin
State Key Laboratory of Coordination Chemistry, MOE Key Laboratory of Mesoscopic Chemistry, MOE Key Laboratory of High Performance Polymer Materials and Technology, Jiangsu Key Laboratory of Advanced Organic Materials, Suzhou Key Laboratory of Green Intelligent Manufacturing of New Energy Materials and Devices, Tianchang New Materials and Energy Technology Research Center, Institute of Green Chemistry and Engineering, School of Chemistry and Chemical Engineering, School of Sustainable Energy and Resources, Nanjing University, Nanjing, Jiangsu 210023, P.R. China
E-mail: zxtie@nju.edu.cn
ychyan@nju.edu.cn
majing@nju.edu.cn
zuojl@nju.edu.cn
zhongjin@nju.edu.cn

Dr. S.-W. Ke[+]
College of Chemistry and Materials Science, Key Laboratory of Functional Molecular Solids, Ministry of Education, Anhui Laboratory of Molecule-Based Materials, Anhui Key Laboratory of Functional Molecular Solids, Anhui Normal University, 189 Jiuhua Southern Road, Wuhu 241002, P.R. China

[+] These authors contributed equally to this work.

Additional supporting information can be found online in the Supporting Information section

metal zinc anodes face their own limitations. The uneven deposition of Zn during battery operation leads to dendrite formation, posing serious risks of short circuits and reduced cycle life.[24–28] In this context, covalent organic frameworks (COFs) offer a promising platform for the design of multifunctional materials. COFs are highly tunable, crystalline materials with well-defined porous structures, enabling the integration of functional building blocks to enhance both conductivity and ion transport.[29–32] However, most COFs still face challenges related to low conductivity and limited electrochemical stability.

Herein, we introduce a novel dual-functional COF, namely Ni–DAPTO, designed to simultaneously address both challenges of cathode conductivity and zinc dendrite formation in AZIBs. By incorporating Ni coordination centers within the COF structure, Ni–DAPTO achieves an expected low energy gap, significantly enhancing its intrinsic electronic conductivity. As a result, Ni–DAPTO as a cathode material demonstrates superior electrochemical performance in AZIBs, delivering a high specific capacity of 127.0 mAh g^{-1} after 10 000 cycles at 0.5 A g^{-1}, and maintaining an excellent specific capacity of 119.7 mAh g^{-1} after 10 000 cycles at a high current density of 10.0 A g^{-1}, with a remarkably low-capacity fade rate of only 0.0012% per cycle. On the other hand, when employed as an artificial solid electrolyte interphase (SEI) layer on the Zn anode, Ni–DAPTO plays a critical role in guiding uniform Zn^{2+} ion deposition and effectively suppressing dendrite formation. The full AZIBs assembled with a Ni–DAPTO cathode and a Ni–DAPTO modified Zn anode exhibit a stable Coulombic efficiency (CE) of over 99% during long-term cycling, with a discharge capacity of 100.9 mAh g^{-1} after 1000 cycles at 5.0 A g^{-1}. The dual-functional performances underscore the intriguing potential of Ni–DAPTO to address both cathode and anode challenges in AZIBs, significantly improving battery longevity, safety, and energy efficiency. This study highlights the design, synthesis, and electrochemical performance of Ni–DAPTO COF, showcasing its promise as a promising material for next-generation AZIBs. By enhancing cathode conductivity and stabilizing the anode against dendrite formation, Ni–DAPTO sets a new benchmark for durable and efficient zinc-ion batteries. The dual-functional design strategy could significantly broaden the application scope of organic electrode materials and stimulate wider research interest in this field.

Results and Discussion

The structures of Ni–bis(dithiolene)-based linker, named Ni–CHO (bis(dithiolene) = bis[1,2-di(4-formylphenyl)ethylene-1,2-dithiolate]) (Figure S1) and 2,7-diaminopyrene-4,5,9,10-tetraone (PTO–$2NH_2$) (Figure S2) were confirmed by hydrogen nuclear magnetic resonance spectroscopy (^{1}H NMR), where both were linked through a Schiff base reaction to bridge redox-active segments with deposition kinetics segments, yielding the dual-functional COF, termed as Ni–DAPTO (Figure 1a).[33] The energy gap of the designed COF was narrowed significantly by introducing the Ni coordination center.[33] Initially, density functional theory (DFT) simulations were employed to analyze the frontier orbital energy levels of Ni–DAPTO. As revealed by the simulated highest occupied crystal orbital (HOCO) and lowest unoccupied crystal orbital (LUCO) energy levels (Figure 1b), the designed Ni–DAPTO achieves the expected low energy gap ($\Delta E_g = 1.68$ eV), substantially lower than those of numerous reported organic electrode materials.[17,34–39] This feature suggests excellent intrinsic electronic conductivity, indicating that Ni–DAPTO is a promising candidate for energy storage material.

Subsequently, the successful synthesis of Ni–DAPTO was verified through comprehensive characterization. In the ^{13}C solid-state NMR spectrum (Figure 1c), the peak at 149.4 ppm clearly confirms the formation of the C=N linkage, while the remaining signals are confidently assigned to carbon atoms in both the benzene ring and the five-membered metallacycle. In the Fourier-transform infrared (FT-IR) spectra (Figure 1d), the peak located at 1662 cm^{-1} is attributed to the C=O stretching vibration of the PTO blocks, which is retained throughout the synthesis process. The disappearance of the stretching vibration peak is attributed to C=O in Ni–CHO (1699 cm^{-1}) and the appearance of the stretching vibration peak is attributed to aliphatic C=N (1620 cm^{-1}), indicating the occurrence of the Schiff base reaction and the successful synthesis of Ni–DAPTO. Similar functional group transformations during the synthesis can also be observed in the Raman spectra within the same frequency range (Figure 1e). Additionally, the D-band and G-band are located at 1395 and 1600 cm^{-1}, respectively, with an I_D/I_G ratio of 0.24, indicating that the structure of Ni–DAPTO is well-ordered. Thermal gravimetric analysis (TGA) was conducted for Ni–DAPTO and its precursor monomers, revealing a decomposition temperature of 410 °C for Ni–DAPTO, verifying its good thermal stability (Figure S3). Morphologies of Ni–DAPTO and its precursors were examined via scanning electron microscopy (SEM). Ni–CHO exhibits a morphology of rod-like crystals with diameters ranging from 1 to 3 μm (Figure S4), while PTO–$2NH_2$ appears as closely packed irregular particles (Figure S5). The Ni–DAPTO product consists of particles with an approximate size of 2 μm (Figure 1f,g). The morphological variations are attributed to the occurrence of polymerization reactions. Changes in the elemental distribution of N, O, S, and Ni further confirm the yield of Ni–DAPTO. More precise elemental analysis also indicates that the elemental mass percentages in Ni–DAPTO are close to the theoretical values (Figure S6).

Further characterization of Ni–DAPTO was performed to elucidate its properties. High-resolution transmission electron microscopy (HR-TEM) images reveal the lattice pattern with a d-spacing of 0.32 nm of Ni–DAPTO (Figures 1h and S7a). The crystallinity of Ni–DAPTO was investigated using powder X-ray diffraction (PXRD) (Figure 1i; Table S1). The sharp peak at 27.9°, as evidenced by the selected area electron diffraction (SAED) pattern obtained from HR-TEM, corresponds to the (001) lattice planes of Ni–DAPTO. The minor peaks observed at 9.5°, 31.4°, and 39.7° are assigned to the (330), (171), and (311) lattice planes, respectively, with corresponding d-spacings of 0.93, 0.285, and 0.23 nm (Figure S7b–d). This indicates the non-uniform crystalline phase of

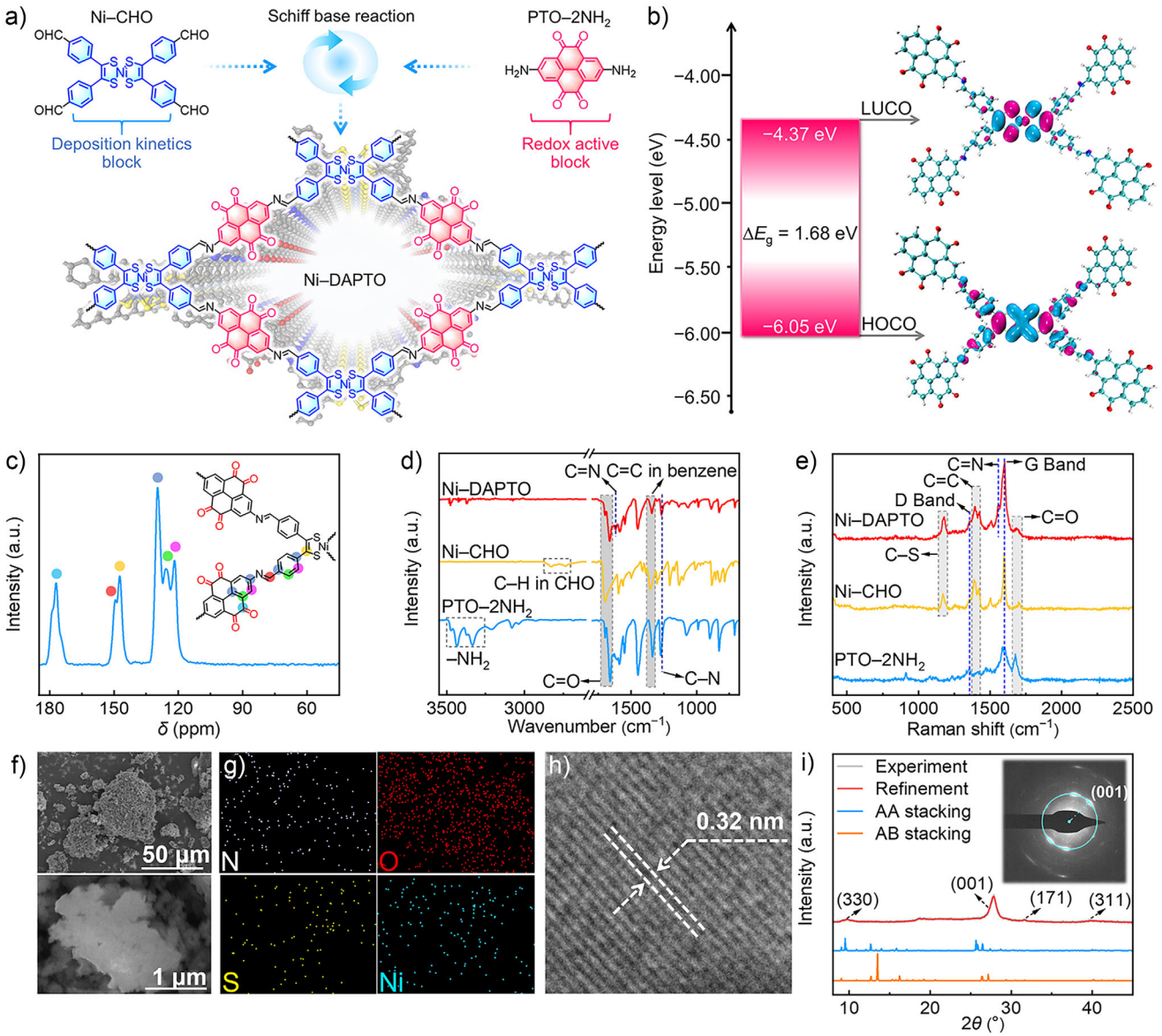

Figure 1. a) The schematic synthesis process of Ni–DAPTO. b) The frontier orbital energy levels of Ni–DAPTO. c) ^{13}C solid-state NMR of Ni–DAPTO. d) FT-IR spectra, and e) Raman spectra of Ni–DAPTO and its precursors. f) SEM images and g) corresponding EDS elemental mappings of Ni–DAPTO. h) The lattice stripe HR-TEM image of Ni–DAPTO. i) PXRD pattern and (the insert) corresponding SAED pattern of Ni–DAPTO.

Ni–DAPTO. The experimental PXRD pattern shows partial consistency with both the AA- and AB-stacking models, suggesting the possible coexistence of both stacking modes. This leads to a mixed lattice arrangement.[40] This phenomenon is attributed to the rapid kinetics of the ammonia-aldehyde condensation reaction coupled with insufficient reversibility. The resulting impairment of molecular reorganization and ordered structural arrangement consequently leads to defect accumulation. The specific surface area and porosity of Ni–DAPTO were analyzed through N_2 adsorption-desorption isotherms at 77.3K (Figure S8a,b), exhibiting a Type II isotherm. According to the Brunauer–Emmett–Teller (BET) method, the specific surface area of Ni–DAPTO is 87.77 $m^2 g^{-1}$, with the pore size distribution dominated by mesopores around 2.90 nm. The CO_2 adsorption-desorption isotherms measured at 195.0K also revealed a similar surface area and pore size (Figure S8c,d). The relatively low surface area is attributed to the non-uniform stacking orientation within the Ni–DAPTO crystals. This structural feature introduces crystallographic defects and reduces the population of long-range-ordered mesopores.[40] These defects facilitate the direct exposure of a greater number of active sites. Solid-state ultraviolet-visible (UV–vis) absorption spectroscopy reveals a direct optical energy gap of 1.96 eV for Ni–DAPTO, which shows good agreement with theoretical calculations (Equation S1; Figure S9). Furthermore, Ni–DAPTO exhibits a measured conductivity of 1.05×10^{-4} S m^{-1}, surpassing most reported organic materials (Equation S2; Figure S10).

When employed as a cathode material, the electrochemical performance of Ni–DAPTO was initially assessed

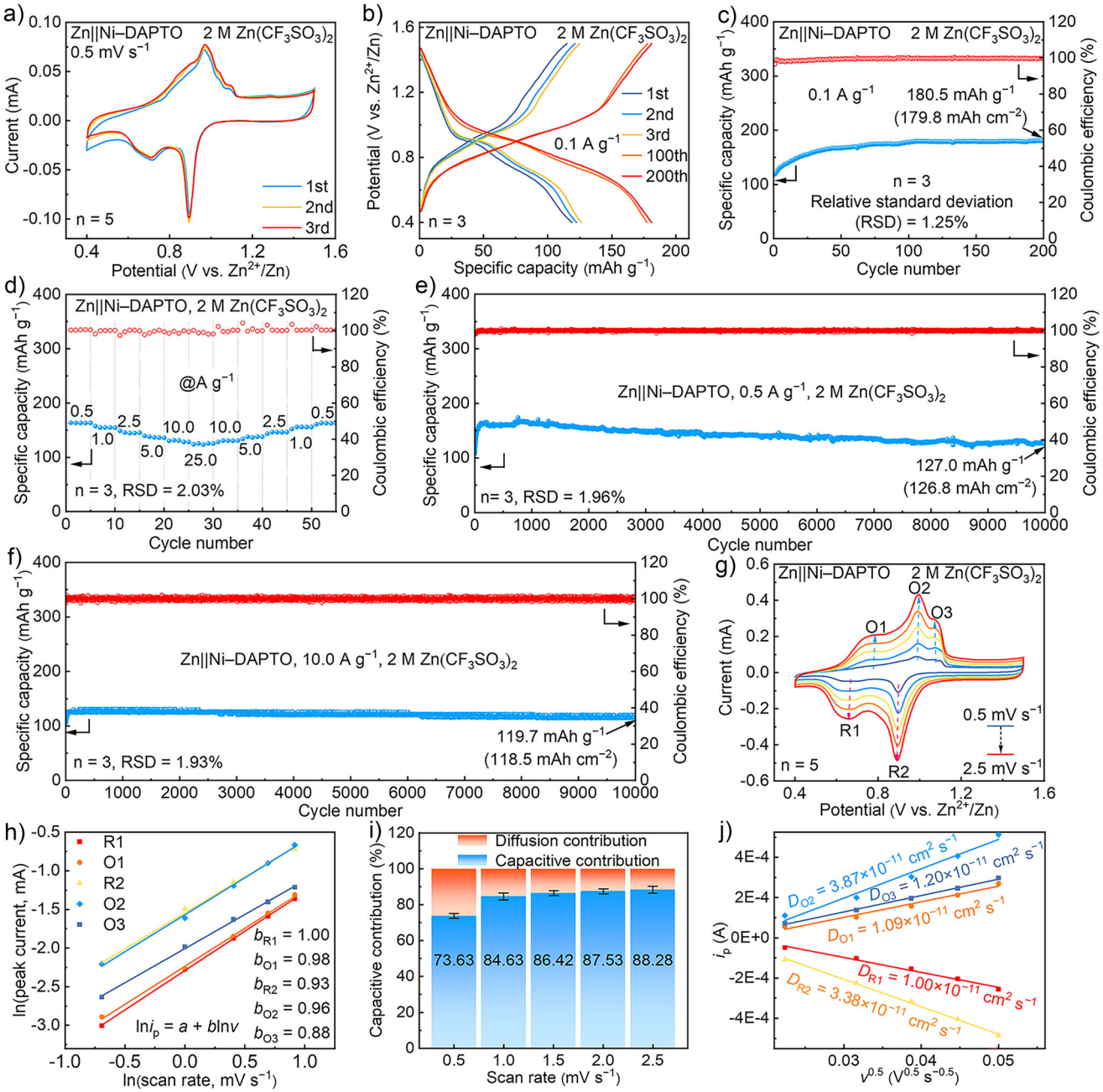

Figure 2. Electrochemical properties of Ni–DAPTO cathode. a) CV curves at 0.5 mV s^{-1}. b) Galvanostatic charge/discharge profiles at 0.1 A g^{-1}. c) Cycling performance at 0.1 A g^{-1}. d) Rate performance. e) Long-term cycling performance at 0.5 and f) 10.0 A g^{-1}. g) CV curves at various scan rates. h) Fitted linear relationship between lni_p and ln$v$ corresponding to (g). i) Capacitive contributions at various scan rates. j) Fitted diffusion coefficients.

via cyclic voltammetry (CV) in the voltage range of 0.4–1.5 V versus Zn^{2+}/Zn. At a scan rate of 0.5 mV s^{-1}, two distinct reduction peaks at 0.90 and 0.72 V (versus Zn^{2+}/Zn) (Figure 2a), corresponding to the sequential reduction of two Zn^{2+} ions with the PTO blocks. Within the voltage range of 0.7–1.1 V (versus Zn^{2+}/Zn), three oxidation peaks were observed, suggesting the reversible release of Zn^{2+} ions. These characteristic oxidation peaks were consistently reproduced in 2.0 M $ZnSO_4$ electrolyte, ruling out anion storage contributions (Figure S11). The overlap of these three oxidation peaks is attributed to the presence of the Ni coordination blocks, which influence the detachment kinetics of Zn^{2+} ions. Galvanostatic discharge/charge profiles at 0.1 A g^{-1} are shown in Figure 2b, and differential capacitance curves (Figure S12) confirm the presence of two discharge plateaus at 0.90 and 0.72 V (versus Zn^{2+}/Zn), with charging plateaus at 0.82 and 0.95 V (versus Zn^{2+}/Zn). These plateaus are well aligned to the reduction and oxidation peaks observed in the CV curves.

During prolonged cycling, the plateaus gradually extend, with a corresponding increase in capacity due to an activation process (Figure 2c) stabilizing at 180.5 mAh g^{-1} after 200

cycles at 0.1 A g^{-1}, reaching 98.3% of the theoretical capacity (C_{th}; Equation S3). This result arises due to enhanced exposure of C=O active sites caused by crystallographic stacking defects, resulting in improved ion accessibility and ultimately higher utilization efficiency. The rate performance of the Ni–DAPTO cathode was tested across a range of current densities from 0.5 to 25.0 A g^{-1}. (Figure 2d). The specific capacities at current densities of 0.5, 1.0, 2.5, 5.0, 10.0, and 25.0 A g^{-1} were 163.4, 155.4, 145.9, 137.4, 129.8, and 124.9 mAh g^{-1}, respectively. Additionally, when the current density was recovered to 0.5 A g^{-1}, the battery exhibited a specific capacity of 162.5 mAh g^{-1} after excluding KB (Figure S13), demonstrating the high reversibility of the redox processes in the Ni–DAPTO cathode. The small capacity difference between low and high current densities reflects the Ni–DAPTO's superior ion transport and fast redox kinetics, facilitated by a short ion transfer path and low energy gap. Notably, continuous cycling at 0.5 A g^{-1} for 10 000 cycles maintained a capacity of 127.0 mAh g^{-1}, representing 69.4% of the C_{th} and 77.0% of the post-activation capacity. The average decay per cycle was merely 0.0039 mAh g^{-1}, with a negligible capacity fade rate of 0.0023% per cycle (Figure 2e). Even under the high-rate condition of 10.0 A g^{-1}, the capacity remained at 119.7 mAh g^{-1} after 10 000 cycles, achieving 65.2% of C_{th} and 94.3% of the capacity at 0.5 A g^{-1} with a capacity fade rate of only 0.0012% per cycle (Figure 2f). The small capacity drop over extended cycling demonstrates the exceptional durability of the Ni–DAPTO, which can be attributed to the synergistic effect of the highly active PTO blocks and the highly conductive Ni coordination blocks. Long-term CE profiles demonstrate values near 100% at both high and low current densities, confirming the exceptional reversibility of the Ni–DAPTO cathode (Figure S14). Occasional CE fluctuations at low rates are attributed to dynamic self-repair of cathode interface passivation layers, while larger CE variations at high rates stem from incomplete double-layer current decay leading to amplified charge/discharge discrepancies. The minimal variations in microstructure and electrode thickness characterized by SEM also indicate the excellent long-cycle stability of the Ni–DAPTO cathode (Figure S15). Moreover, even at a high mass loading of 6.8 mg cm^{-2}, the Ni–DAPTO cathode still delivers a notable specific capacity of 69.6 mAh g^{-1} after 100 cycles at 0.5 A g^{-1} (Figure S16). Remarkably, Ni–DAPTO maintains stable cycling performances under both relatively low and high temperatures (−10° and 50 °C), demonstrating exceptional environmental endurance (Figure S17). Compared to previously reported organic cathodes employing other optimization strategies, Ni–DAPTO exhibits superior intrinsic conductivity and rate stability (Table S2).[16,17,19,34–39] The enhanced performance underscores the rational design approach for Ni–DAPTO, highlighting its potential as a promising cathode material for battery systems.

The configuration of highly active blocks alongside low energy gap blocks in Ni–DAPTO not only benefits excellent capacity and cycling stability but also provides rapid redox kinetics. To investigate the kinetics of the Ni–DAPTO cathode, CV scans were performed at 0.5, 1.0, 1.5, 2.0, and 2.5 mV s^{-1} (Figure 2g). Fitting the peak current (i_p) versus scan rate (v) according to Equations S4 and S5 reveals a linear relationship (Figure 2h), with b-values of 1.00 and 0.93 for the reduction peaks and 0.98, 0.96, and 0.88 for the oxidation peaks, indicating that the kinetic behavior during the discharge/charge process is dominated by surface-controlled capacitive behavior. Further quantification of the capacitive capacity contribution via Equations S6–S8 shows that the capacitive contributions at different scan rates are 73.63%, 84.63%, 86.42%, 87.53%, and 88.28% (Figures 2i and S18; Table S3), consistent with the fitting results in Figure 2h. The high capacitive contributions are attributed to the diffusion barriers caused by the large ionic radius and high charge density of Zn^{2+} ions. At high scan rates/current densities, the faster-responding pseudocapacitive and electric double-layer processes become dominant. This characteristic phenomenon in aqueous batteries effectively meets the requirements for rapid charge/discharge applications. Finally, the diffusion coefficients of Zn^{2+} were calculated by the Randles–Sevcik equation (Equation S9). As shown in Figure 2j, the diffusion coefficients for the reduction peaks are 1.00×10^{-11} and 3.38×10^{-11} cm^2 s^{-1}, and for the oxidation peaks, they are 1.09×10^{-11}, 3.87×10^{-11}, and 1.20×10^{-11} cm^2 s^{-1}. The rapid redox kinetics of Ni–DAPTO cathode is mainly attributed to the low energy gap and superior intrinsic electronic conductivity provided by the Ni coordination blocks.

To elucidate the zinc ion storage mechanism of Ni–DAPTO as a cathode in AZIBs, in situ Raman spectra were initially employed to monitor the structural changes in Ni–DAPTO during the discharge/charge processes (Figure S19). In the three-dimensional plot (Figure 3a), there is a noticeable intensity reduction at 1680 cm^{-1}, attributed to the C=O bond. The corresponding isosurface plot (Figure 3b) shows that the intensity of the characteristic peak of C=O gradually decreases during the discharge process and subsequently increases during the following charge process. This result suggests the reversible transformation of C=O groups in the CV curves, indicating their critical role in Zn^{2+} ion binding and release, forming the basis of the redox reaction during cycling. Furthermore, the in situ PXRD patterns demonstrate that the characteristic peaks at 27.9° and 9.5° remain stable throughout electrochemical cycling, confirming the structural integrity and robustness of Ni–DAPTO during charge/discharge processes (Figure S20).

To further understand the energy storage process involving C=O, ex situ high-resolution XPS spectra at O 1s and Zn 2p regions of the Ni–DAPTO cathode at various states of charge were characterized (Figure 3c and Table S4). In the pristine electrode, the characteristic peak for C=O was observed at 531.8 eV in the O 1s region, with no detectable Zn signals. Upon discharging to 0.81 V (versus Zn^{2+}/Zn), the intensity of the C=O peak significantly diminishes, and a new peak corresponding to C–O (532.9 eV) emerges, alongside the appearance of Zn···O peaks (at 1046.2 and 1023.2 eV). This indicates that Zn^{2+} ions coordinate with the C=O groups, forming a C–O···Zn···O–C structure during the reduction process. After fully discharging to 0.40 V (versus Zn^{2+}/Zn), the C=O peak completely transforms into C–O, with the Zn···O peaks being retained, confirming that two Zn^{2+} ions are involved in the reduction reaction. During

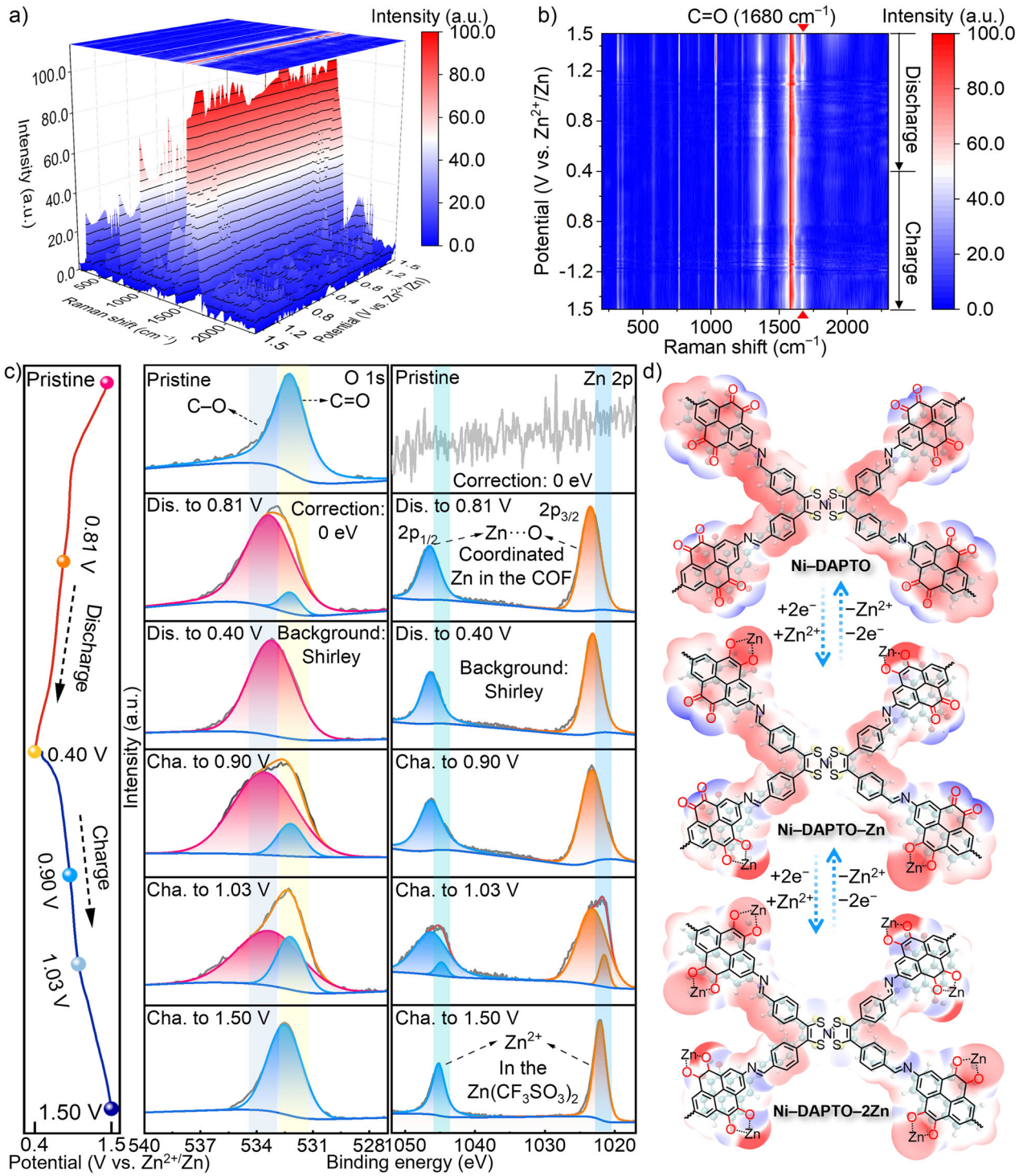

Figure 3. a) In situ Raman analyses and b) corresponding Raman contour map of Ni–DAPTO cathode at various charge/discharge states. c) High-resolution XPS spectra at O 1s and Zn 2p regions of Ni–DAPTO cathode at various charge/discharge states. d) Proposed Zn^{2+} ion storage mechanism and corresponding MESP distribution in the repetitive unit of Ni–DAPTO.

subsequent charging, the C=O peak reappeared, with the Zn···O signal diminishing, accompanied by the emergence of peaks corresponding to free Zn^{2+} (at 1045.0 and 1022.0 eV), indicating the detachment of Zn^{2+} ions from the coordination structure. Fully charging to 1.5 V (versus Zn^{2+}/Zn) results in the complete transformation of C–O back to C=O, and the Zn···O peaks fully revert to Zn^{2+} peaks in $Zn(CF_3SO_3)_2$ salt, demonstrating the complete detachment of Zn^{2+} from the C–O···Zn···O–C structure. This also indicates that the oxidation peak at 1.1 V (versus Zn^{2+}/Zn) involves Zn^{2+} ions, which is due to the delayed detachment of Zn^{2+} ions. The mutual transformation of C=O to C–O observed in the XPS

spectra, along with the shifts in the characteristic peaks of Zn 2p, indicate that the energy storage mechanism of the Ni–DAPTO cathode involves a reversible redox reaction with two Zn^{2+} ions and the C=O groups in the PTO blocks. Additionally, the absence of the C–O–H characteristic peak at 530.4 eV indicates that H^+ ions do not participate in the charge storage processes. The unchanged characteristics of the N 1s and Ni 2p XPS spectra between the pristine and fully discharged states of the Ni–DAPTO cathode demonstrate the electrochemical inertness of both the C=N groups and Ni coordination centers within this battery system (Figure S21).

Molecular electrostatic potential (MESP) analysis of Ni–DAPTO (Figure 3d) visually demonstrates that the regions of maximum negative potential are concentrated around the C=O groups, indicating that these sites are highly favorable for Zn^{2+} ion adsorption.[41,42] During the initial reduction stage, one Zn^{2+} ion is coordinated by two C=O groups on the same side of the PTO block, forming a C–O···Zn···O–C structure. As the discharge continues, a second Zn^{2+} ion is bonded by the remaining C=O groups on the opposite side, completing the reduction process. Moreover, the significantly more negative MESP minimum at C=O sites (average = −40.90 kcal mol^{-1}) compared to C=N groups (average = −14.99 kcal mol^{-1}) indicates substantially lower reducibility/reactivity of the C=N functionality. (Figure S22). Both experimental characterization and theoretical calculation results indicate that the Zn^{2+} ions storage mechanism in the Ni–DAPTO cathode involves the sequential binding of two Zn^{2+} ions into the C=O groups on both sides of the PTO blocks, constituting a reversible four-electron process.

In addition to its role as a high-performance cathode material, Ni–DAPTO also can function as an effective artificial SEI layer for Zn anode. Compared to traditional COF-based SEIs, the combination of nickel coordination blocks and zincophilic sites endows the SEI with excellent mechanical strength and chemical stability.[43–45] This pairing not only enhances electronic conductivity but also precisely controls the zinc ion transport pathways. Table S5 presents DFT-computed Zn^{2+} deposition energies on functional fragments of Ni–DAPTO as an artificial anodic SEI (Equation S10). Operating outside the redox potential window of C=O in the PTO block, Ni–DAPTO avoids cathodic redox reactions. Thus, when serving as anodic SEI, the C=O groups in Ni–DAPTO contribute through high zincophilicity rather than redox activity. Meanwhile, Zn^{2+} spontaneously migrates from S sites to Ni sites, achieving comparable deposition energy to Ni sites (−2.08 eV), while C=N shows minimal deposition energy. This indicates that the Ni coordination blocks can function as an ideal substrate for guiding the uniform nucleation and regulating the homogeneous deposition of Zn^{2+} ions. To experimentally confirm this, the Ni–DAPTO was coated onto a Cu current collector (Ni–DAPTO/Cu), and Zn||Cu half-batteries were assembled for testing (Figure 4a). The Zn||Cu half-cell with Ni–DAPTO/Cu current collector demonstrated a significantly higher CE of 99.00% after 20 cycles compared to 97.12% for the bare Cu counterpart, clearly indicating the improved Zn deposition efficiency due to the Ni–DAPTO guiding layer. Further examination in the insert (Figure 4b) reveals that the Ni–DAPTO/Cu current collector demonstrates a lower polarization voltage compared to bare Cu. In the CE tests of Zn||Cu half-batteries at a current density of 1.0 mA cm^{-2} and a capacity of 1.0 mAh cm^{-2} (Figure 4c), the Ni–DAPTO/Cu current collector also showed a long lifespan and good cycling stability, maintaining a CE of 99.2% after 300 deposition/stripping cycles. In contrast, the CE of the bare Cu current collector dropped to zero after only 94 cycles. The significant advantage of Ni–DAPTO/Cu in CE indicates that the Ni–DAPTO coating can substantially promote the rapid and uniform deposition/stripping of Zn, thereby guiding uniform Zn deposition and ultimately achieving higher Zn utilization (Equation S11). Furthermore, mass transfer and nucleation overpotential tests (Figures 4d and S23) demonstrated the efficacy of the Ni–DAPTO/Cu system. The mass transfer overpotential and nucleation overpotential for Ni–DAPTO/Cu were found to be significantly lower (26.1 and 22.3 mV (versus Zn^{2+}/Zn)) compared to bare Cu at 72.0 and 57.0 mV (versus Zn^{2+}/Zn) which highlights the superior ion mobility and reduced Zn plating barrier provided by the Ni–DAPTO framework. Additionally, the voltage profiles for Zn deposition/stripping on Ni–DAPTO/Cu and bare Cu current collectors at a current density of 1.0 mA cm^{-2} were thoroughly studied (Figure S24). By comparing the polarization voltages at the 80th cycle, it was found that the battery using Ni–DAPTO/Cu exhibited an ultralow polarization potential of 48.6 mV (versus Zn^{2+}/Zn), whereas the bare Cu counterpart demonstrated a significantly higher polarization potential of 581.2 mV (versus Zn^{2+}/Zn). Even after 100 cycles, the battery based on Ni–DAPTO/Cu continued to show high Zn utilization efficiency, low polarization voltage, and nearly identical voltage profiles, indicating stable and efficient Zn cycling over time. Moreover, electrochemical impedance spectroscopy (EIS) tests of the Zn||Cu half-batteries (Figure 4e; Table S6) confirmed that both the electrolyte resistance and interfacial resistance of the battery based on the Ni–DAPTO/Cu current collector are significantly lower both before and after 100 h of cycling, compared to the bare Cu-based battery. This demonstrates the ability of the Ni–DAPTO coating to significantly reduce internal resistance and facilitate ion transfer during extended cycling. In the CV tests of the Zn||Cu half-batteries (Figure 4f), the Cu electrode coated with Ni–DAPTO exhibited higher response currents during the deposition/stripping processes (59.09 mA cm^{-2}/54.69 mA cm^{-2}) than bare Cu (35.14 mA cm^{-2}/35.66 mA cm^{-2}). The nucleation overpotential (19.70 mV) closely matches the result observed in Figure 4d. The rapid deposition and stripping of Zn^{2+} ions originate from the selective adsorption of Zn^{2+} ions by the Ni–S coordination sites in Ni–DAPTO, corroborating the DFT calculation results. Additionally, the highly redox-active PTO blocks provide abundant zincophilic sites that synergistically enhance zinc migration.

To visually elucidate the impact of the Ni–DAPTO artificial SEI on the Zn deposition morphology and Zn dendrite suppression, SEM studies were conducted on the morphological evolution of different Cu electrodes recovered from Zn||Ni–DAPTO/Cu and Zn||bare Cu half-cells after 100 h of cycling. The post-cycling Ni–DAPTO/Cu electrode (Figures 4g and S25) retained a smooth and dense surface, with the characteristic layered structure of the COF clearly

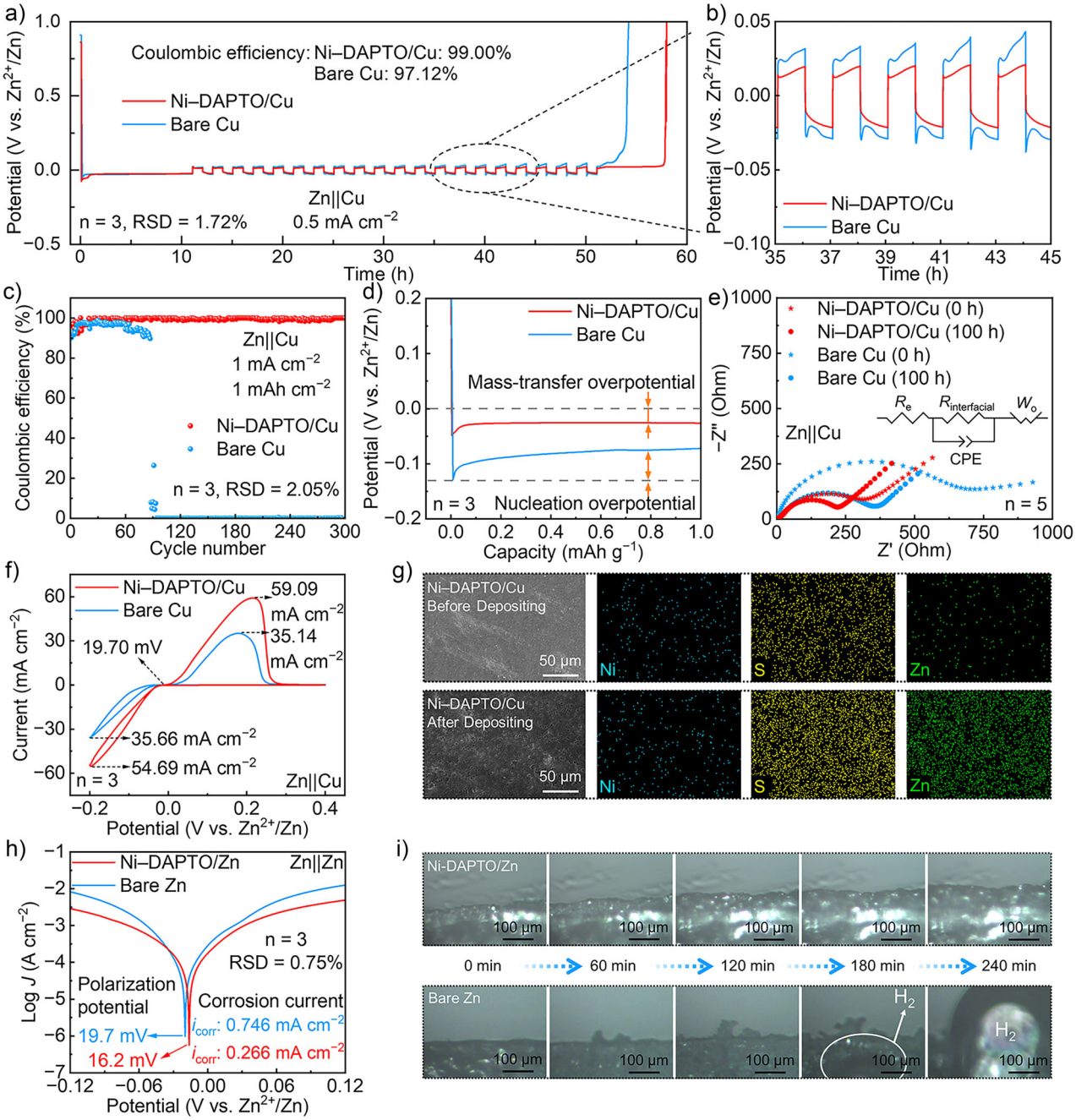

Figure 4. Electrochemical performances of Zn||Cu half batteries with Ni–DAPTO/Cu and bare Cu current collectors, and Zn||Zn symmetrical batteries with Ni–DAPTO/Zn and bare Zn anodes. a), b) Potential-time curves of Zn||Cu half batteries to calculate the average CEs at a current density of 0.5 mA cm^{-2}. c) CE tests for long-term cycling of Zn||Cu half batteries at 1.0 mA cm^{-2} with a capacity of 1.0 mA h cm^{-2}. d) Potential profiles during the initial Zn plating process of two different current collectors. e) Nyquist plots of Zn||Cu half batteries. The inset image is the equivalent circuit diagram. f) CV curves of Zn||Cu half batteries at a scan rate of 1.0 mV s^{-1} from 0.2 to 0.4 V (versus Zn2+/Zn). g) SEM images of Ni–DAPTO/Cu electrodes retrieved from Zn||Cu half batteries cycling at 1.0 mA cm^{-2} before and after 50 cycles, and corresponding EDS mappings of Ni, S, and Zn elements. h) Tafel curves of Zn||Zn symmetrical batteries. i) In situ microscopy images of the Zn plating process on (top) Ni–DAPTO/Zn and (bottom) the bare Zn anode.

visible. This structure facilitated uniform Zn deposition, as indicated by the homogeneous distribution of Zn elements. The increase in O and S elements originated from the $Zn(CF_3SO_3)_2$ electrolyte. In contrast, top-view and cross-sectional SEM images of the bare Cu current collector (Figures S26 and S27) at various scales revealed a loose, rough surface with prominent cracks. Further magnified SEM images reveal vertically grown Zn dendrites and extensive aggregated "dead" Zn fully covering the electrode surface, indicating severe electrolyte corrosion. After 100 h of cycling, the natural SEI structure of the bare Cu electrode was entirely degraded, resulting in an unstable and damaged electrode

surface. The cross-sectional SEM also shows that there is obvious dendrite growth on the Cu surface. The Ni–DAPTO artificial SEI, however, effectively guides Zn to grow laterally during the deposition/stripping process, which inhibits Zn dendrite growth and extends the cycle stability of batteries.

To further highlight the protective effect of the Ni–DAPTO COF layer on the Zn anode, Zn||Zn symmetric batteries were assembled and tested using Ni–DAPTO coated Zn (Ni–DAPTO/Zn) electrodes. Initially, symmetric batteries based on both Ni–DAPTO/Zn and bare Zn electrodes were cycled at different current densities ranging from 0.2 to 5.0 mA cm^{-2}, with a fixed capacity of 1.0 mAh cm^{-2} (Figures S28 and S29). As the current density increased, both types of batteries showed rising overpotentials. However, when the current density reached 2 mA cm^{-2}, the battery based on bare Zn electrodes suffered a short circuit due to the irreversible growth of Zn dendrites piercing the separator. In contrast, the symmetric battery with Ni–DAPTO/Zn electrodes sustained stable plating/stripping processes at various current densities, consistently maintaining a lower overpotential. Subsequently, Tafel plots were obtained for the Zn||Zn symmetric batteries (Figure 4h). Compared to bare Zn, the battery using Ni–DAPTO/Zn electrodes displayed a lower corrosion current density (0.266 mA cm^{-2}) and polarization voltage (16.2 mV versus Zn^{2+}/Zn), indicating that the Ni–DAPTO layer significantly enhances the corrosion resistance of the Zn electrode. In the hydrogen evolution reaction (HER) tests, the Ni–DAPTO interphase induced a cathodic shift of HER potential from −0.048 V (versus Zn^{2+}/Zn) (for bare Zn) to −0.078 V (versus Zn^{2+}/Zn) (for Ni–DAPTO/Zn), demonstrating suppressed hydrogen evolution at Zn anodes (Figure S30).

To directly observe the electro-deposition behavior of Zn^{2+} ions on the anode, an in situ optical characterization method was employed. The in situ growth process of Zn was observed under an optical microscope for a deposition time of 6 h (Figure 4i). Throughout the deposition process, the surface of Ni–DAPTO/Zn electrode remained flat and smooth, with no significant protrusions and no HER observed. In contrast, the bare Zn surface showed Zn protrusions after just 1 h, hydrogen bubbles appeared after 3 h, and by 6 h, these bubbles had enlarged, covering the entire field of view. These observations confirm that the Ni–DAPTO artificial SEI plays a critical role in inducing the uniform deposition of Zn^{2+} ions, suppressing the growth of Zn dendrites, and inhibiting the unwanted HER. This effect is attributed to the selective adsorption of Zn^{2+} ions by the Ni–S coordination sites within the Ni–DAPTO framework, while the zincophilic PTO blocks synergistically enhance charge transfer kinetics. Together, these features enable the rapid and uniform deposition of Zn^{2+} ions. Additionally, the simulated calculations also indicate that in the pores of Ni–DAPTO, the migration barrier of $CF_3SO_3^-$ anions (3.3×10^{-3} eV) is nearly two orders of magnitude higher than that of Zn^{2+} (5.2×10^{-5} eV) (Figure S31). It suggests that the microporous structure of Ni–DAPTO allows for efficient electrolyte permeation, enhancing the ionic conductivity of the COF layer. The micropores of Ni–DAPTO can also selectively block larger $CF_3SO_3^-$ anions while permitting the transport of Zn^{2+} ions, thereby reducing the corrosion of the Zn metal, homogenizing the Zn flux, and facilitating uniform Zn deposition.[33]

To demonstrate the critical role of Ni–DAPTO artificial SEI in inducing the uniform deposition of Zn^{2+} ions and suppressing Zn dendrite growth, specially designed full batteries with limited Zn anodes were assembled and evaluated (Figure 5a). Specifically, following 50 cycles in Zn||Cu half-batteries, a Zn layer of 5.0 mAh cm^{-2} was deposited onto Ni–DAPTO/Cu and bare Cu current collectors, designated as Zn@Ni–DAPTO/Cu and Zn@bare Cu anodes, respectively. Subsequently, the Cu electrodes plated with Zn were retrieved and used as limited-Zn anodes to assemble full batteries. As shown in Figure 5b, a substantial difference in long-term cycling stability was observed. The Zn@Ni–DAPTO/Cu||Ni–DAPTO full battery exhibited a markedly extended cycle life with improved CE, maintaining a notable discharge capacity of 100.9 mAh g^{-1} even after 1000 cycles at a current density of 5.0 A g^{-1}, with a capacity retention of 68.03%. In sharp contrast, the Zn@bare Cu||Ni–DAPTO full battery suffered rapid capacity fading, with the CE dropping below 99.0% after 500 cycles, retaining only 52.4 mAh g^{-1} of discharge capacity. By 1000 cycles, the discharge capacity had nearly diminished to zero. These pronounced differences in full-battery cycling performance stem from the distinct surface morphologies of the Zn anodes. Benefiting from the protective effect of Ni–DAPTO on the Zn anode, the utilization of Zn in the battery was significantly enhanced, leading to the outstanding cycling stability of the full battery.

Additionally, rate performance tests were conducted on Zn@Ni–DAPTO/Cu||Ni–DAPTO and Zn@bare Cu||Ni–DAPTO full batteries across different current densities ranging from 0.1 to 5.0 A g^{-1} (Figure 5c–e). Compared to Zn@bare Cu, the full battery based on the Zn@Ni–DAPTO/Cu anode demonstrated superior rate capability. When the current density returned to 0.1 A g^{-1}, the battery with the Zn@Ni–DAPTO/Cu anode maintained high cycling stability, with the discharge capacity recovering to 141.2 mAh g^{-1}, whereas the capacity of the Zn@bare Cu-based battery only returned to 117.5 mAh g^{-1}. The rapid capacity decay is attributed to the low utilization of Zn due to dendrite formation on the Zn@bare Cu electrode at high current densities, further substantiating the significant role of Ni–DAPTO artificial SEI in enhancing the cycling performance of the battery.

To further demonstrate the practical application potential of Ni–DAPTO, a pouch battery based on a Zn anode modified with Ni–DAPTO (Ni–DAPTO/Zn||Ni–DAPTO) was assembled (Figure 5f). At 0.2 A g^{-1}, the initial discharge capacity was 167.7 mAh g^{-1}, with corresponding energy and power densities of 39.7 and 47.4 W kg^{-1}, respectively (Figure S32; Equations S12–S14). Even after 300 cycles, the battery maintained a high discharge capacity of 92.3 mAh g^{-1} (21.7 and 47.0 W kg^{-1}). XPS characterizations of the Ni–DAPTO/Zn anode before and after cycling reveal unaltered C=O signatures alongside substantial binding energy upshifts and peak broadening in the Ni 2p region (Figure S33). This phenomenon is attributed to massive Zn^{2+} adsorption at Ni coordination centers, which alters the local electron density around Ni sites. These findings confirm the absence of

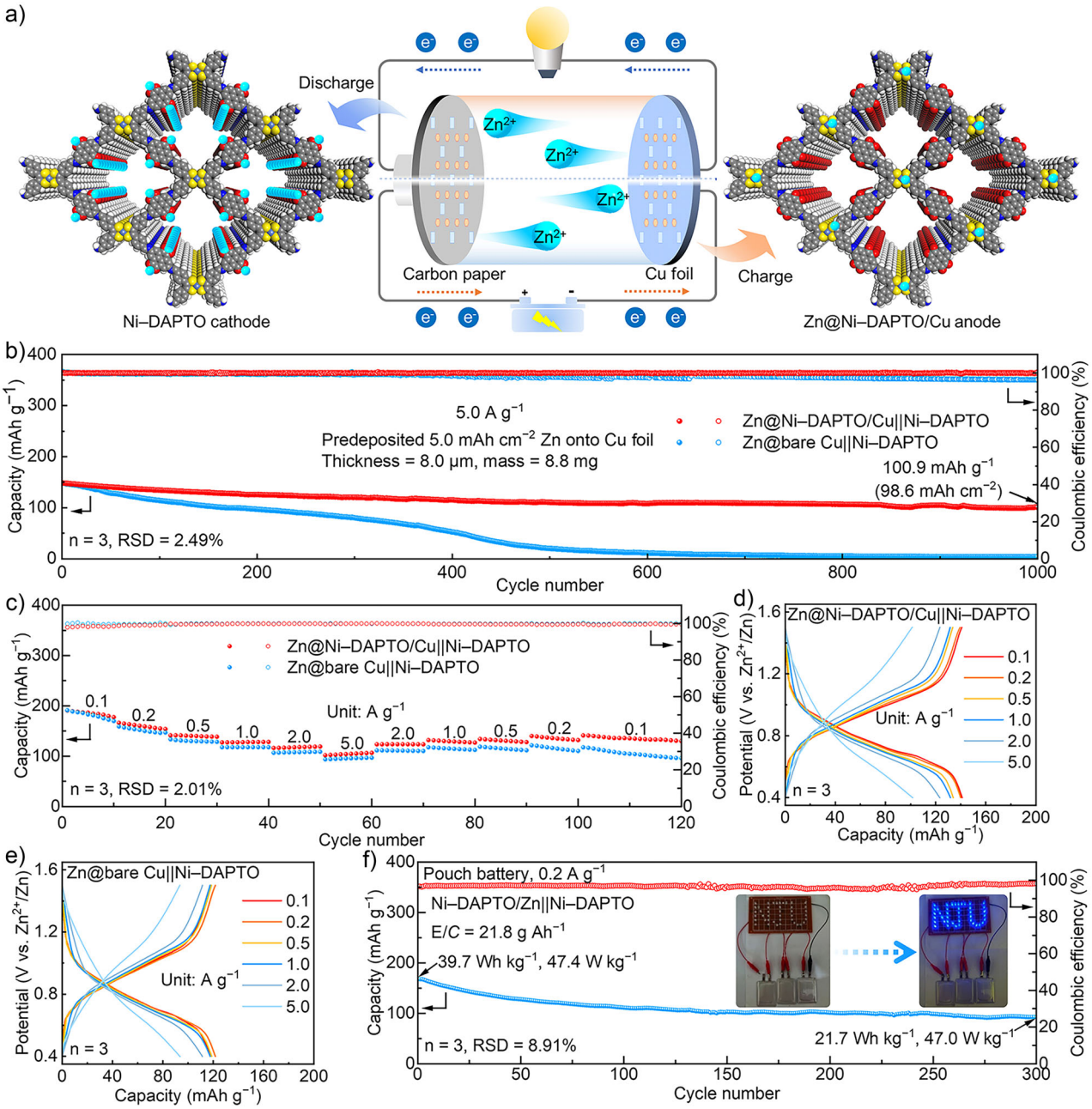

Figure 5. a) Operation mechanism diagram of Ni–DAPTO for both Zn2+ storage and Zn deposition control for AZIBs. b) Cycling performances of Zn@Ni–DAPTO/Cu||Ni–DAPTO and Zn@bare Cu||Ni–DAPTO full batteries at a current density of 5.0 A g^{-1}. c) Rate performances of full batteries at various current densities from 0.1 to 5.0 A g^{-1}. d), e) Galvanostatic charge/discharge profiles of full batteries assembled with (d) Zn@Ni–DAPTO/Cu and (e)Zn@bare Cu anodes at various current densities from 0.1 to 5.0 A g^{-1}. f) Cycling performances of Zn@Ni–DAPTO/Cu||Ni–DAPTO pouch battery at a current density of 0.2 A g^{-1}. The insert in (f) shows three series-connected pouch batteries powering a light-emitting diode (LED) panel.

significant material degradation while demonstrating that Ni coordination centers serve as the primary active sites governing zinc deposition behavior. The corresponding SEM images reveal that Zn deposits conformally across the Ni–DAPTO layer, completely filling the interparticle spaces within the Ni–DAPTO matrix (Figure S34). Additionally, three of these pouch cells connected in series successfully powered an LED light panel, illustrating the practical application potential of Ni–DAPTO as an artificial SEI for Zn anodes.

Conclusion

This study presents Ni–DAPTO, a dual-functional COF that simultaneously addresses two key challenges in AZIBs: the low conductivity in organic cathode materials and the zinc dendrite formation on the anode. The low energy gap of Ni–DAPTO, combined with its Ni coordination centers, enables both high conductivity and the uniform deposition of Zn^{2+} ions. As a result, the Ni–DAPTO cathode exhibits exceptional

cycling performance and stability with remarkable rate capability under high-rate conditions. More importantly, on the anode side, Ni–DAPTO as an artificial SEI layer can effectively guide the uniform deposition of Zn, significantly enhancing the cycling stability and CE of Zn anodes. The full batteries and pouch batteries based on Ni–DAPTO demonstrate excellent cycling performance, validating the substantial potential of the Ni–DAPTO for practical applications. We firmly believe the dual-functional COF design strategy possesses universal applicability, with its foremost advantage being the capacity for customizable molecular engineering tailored to specific battery system requirements. Moreover, this design paradigm need not be confined to metal-ion systems or dual functionalities; future research may extend it to non-metal-ion systems and triple-function or even multifunctional architectures. This work introduces a novel approach to realizing advanced AZIBs by utilizing rationally designed COF materials, specifically through the construction of multifunctional, modular structures via precise structural editing, holding significant potential to propel innovation and development in aqueous rechargeable battery technology.

Acknowledgements

The authors appreciate the financial support from the National Natural Science Foundation of China (22479074, 22475096, 22494633 and 22275084), the Equipment Pre-Research and Ministry of Education Joint Fund General Project (8091B02052407), the Natural Science Foundation of Jiangsu Province (BK20240400, BK20241236 and BK20243010), the Science and Technology Major Project of Jiangsu Province (BG2024013), the Scientific and Technological Achievements Transformation Special Fund of Jiangsu Province (BA2023037), the Academic Degree and Postgraduate Education Reform Project of Jiangsu Province (JGKT24_C001), the Key Core Technology Open Competition Project of Suzhou City (SYG2024122), the Open Research Fund of Suzhou Laboratory (SZLAB-1308–2024-TS005), the Gusu Leading Talent Program of Scientific and Technological Innovation and Entrepreneurship in Wujiang District of Suzhou City (ZXL2021273), and the Chenzhou National Sustainable Development Agenda Innovation Demonstration Zone Provincial Special Project (2023sfq11).

Conflict of Interests

The authors declare no conflict of interest.

Data Availability Statement

The data that support the findings of this study are available from the corresponding author upon reasonable request.

Keywords: Covalent organic frameworks · Dual function · Organic cathode · Rechargeable zinc-ion batteries · Zn deposition control

[1] M. Armand, J.-M. Tarascon, *Nature* **2008**, *451*, 652–657.
[2] B. Niu, J. Wang, Y. Guo, Z. Li, C. Yuan, A. Ju, X. Wang, *Adv. Energy Mater.* **2024**, *14*, 2303967.
[3] H. Lu, S. Meng, T. He, C. Zhang, J. Yang, *Coord. Chem. Rev.* **2024**, *514*, 215910.
[4] J. Zhu, Z. Bie, X. Cai, Z. Jiao, Z. Wang, J. Tao, W. Song, H. J. Fan, *Adv. Mater.* **2022**, *34*, e2207209.
[5] K. Zhang, Y. Ge, Q. Yu, P. Zhang, Y. Feng, Z. Tie, J. Ma, Z. Jin, *Energy Storage Mater.* **2024**, *67*, 103296.
[6] K. Zhang, Q. Yu, J. Sun, Z. Tie, Z. Jin, *Adv. Mater.* **2024**, *36*, e2309838.
[7] Y. Zhu, G. Liang, X. Cui, X. Liu, H. Zhong, C. Zhi, Y. Yang, *Energy Environ. Sci.* **2024**, *17*, 369–385.
[8] L. Ma, S. Chen, N. Li, Z. Liu, Z. Tang, J. A. Zapien, S. Chen, J. Fan, C. Zhi, *Adv. Mater.* **2020**, *32*, e1908121.
[9] J. Yang, B. Yin, Y. Sun, H. Pan, W. Sun, B. Jia, S. Zhang, T. Ma, *Nano-Micro Lett.* **2022**, *14*, 42.
[10] M. Chen, S. Xie, X. Zhao, W. Zhou, Y. Li, J. Zhang, Z. Chen, D. Chao, *Energy Storage Mater.* **2022**, *51*, 683–718.
[11] Y. Lu, Y. Cai, Q. Zhang, J. Chen, *Adv. Mater.* **2022**, *34*, 2104150.
[12] Q. Yu, Z. Xue, M. Li, P. Qiu, C. Li, S. Wang, J. Yu, H. Nara, J. Na, Y. Yamauchi, *Adv. Energy Mater.* **2021**, *11*, 2002523.
[13] Z. Chen, H. Cui, Y. Hou, X. Wang, X. Jin, A. Chen, Q. Yang, D. Wang, Z. Huang, C. Zhi, *Chem* **2022**, *8*, 2204–2216.
[14] H. Peng, Q. Yu, S. Wang, J. Kim, A. E. Rowan, A. K. Nanjundan, Y. Yamauchi, J. Yu, *Adv. Sci.* **2019**, *6*, 1900431.
[15] A. Vlad, J. Chen, Y. Yao, *Batteries Supercaps* **2023**, *6*, e202300090.
[16] Q. Zhao, W. Huang, Z. Luo, L. Liu, Y. Lu, Y. Li, L. Li, J. Hu, H. Ma, J. Chen, *Sci. Adv.* **2018**, *4*, eaao1761.
[17] Z. Tie, L. Liu, S. Deng, D. Zhao, Z. Niu, *Angew. Chem. Int. Ed.* **2020**, *132*, 4950–4954.
[18] N. Wang, X. Dong, B. Wang, Z. Guo, Z. Wang, R. Wang, X. Qiu, Y. Wang, *Angew. Chem. Int. Ed.* **2020**, *59*, 14577–14583.
[19] Y. Wang, C. Wang, Z. Ni, Y. Gu, B. Wang, Z. Guo, Z. Wang, D. Bin, J. Ma, Y. Wang, *Adv. Mater.* **2020**, *32*, e2000338.
[20] P. Poizot, J. Gaubicher, S. Renault, L. Dubois, Y. Liang, Y. Yao, *Chem. Rev.* **2020**, *120*, 6490–6557.
[21] Y. Chen, C. Wang, *Acc. Chem. Res.* **2020**, *53*, 2636–2647.
[22] Y. Lu, Q. Zhang, L. Li, Z. Niu, J. Chen, *Chem* **2018**, *4*, 2786–2813.
[23] B. Lee, Y. Ko, G. Kwon, S. Lee, K. Ku, J. Kim, K. Kang, *Joule* **2018**, *2*, 61–75.
[24] J. Cao, X. Wang, S. Qian, D. Zhang, D. Luo, L. Zhang, J. Qin, X. Zhang, X. Yang, J. Lu, *Adv. Mater.* **2024**, *36*, e2410947.
[25] Y. Meng, M. Wang, J. Wang, X. Huang, X. Zhou, M. Sajid, Z. Xie, R. Luo, Z. Zhu, Z. Zhang, N. A. Khan, Y. Wang, Z. Li, W. Chen, *Nat. Commun.* **2024**, *15*, 8431.
[26] F. Zhang, J. Qian, W. Dong, Y. Qu, K. Chen, J. Chen, Y. Cui, L. Chen, *Energy Environ. Sci.* **2024**, *17*, 7258–7270.
[27] Z. Zheng, X. Zhong, Q. Zhang, M. Zhang, L. Dai, X. Xiao, J. Xu, M. Jiao, B. Wang, H. Li, Y. Jia, R. Mao, G. Zhou, *Nat. Commun.* **2024**, *15*, 753.
[28] T. Huang, K. Xu, N. Jia, L. Yang, H. Liu, J. Zhu, Q. Yan, *Adv. Mater.* **2023**, *35*, e2205206.
[29] A. P. Coˆte´, A. I. Benin, N. W. Ockwig, M. O'Keeffe, A. J. Matzger, O. M. Yaghi, *Science.* **2005**, *310*, 1166–1170.
[30] S. Kandambeth, K. Dey, R. Banerjee, *J. Am. Chem. Soc.* **2019**, *141*, 1807–1822.
[31] R. Dantas, C. Ribeiro, M. Souto, *Chem. Commun.* **2023**, *60*, 138–149.
[32] S. Haldar, M. Wang, P. Bhauriyal, A. Hazra, A. H. Khan, V. Bon, M. A. Isaacs, A. De, L. Shupletsov, T. Boenke, J. Grothe, T. Heine, E. Brunner, X. Feng, R. Dong, A. Schneemann, S. Kaskel, *J. Am. Chem. Soc.* **2022**, *144*, 9101–9112.

[33] S. W. Ke, Y. Wang, J. Su, K. Liao, S. Lv, X. Song, T. Ma, S. Yuan, Z. Jin, J. L. Zuo, *J. Am. Chem. Soc.* **2022**, *144*, 8267–8277.
[34] W. Wang, V. S. Kale, Z. Cao, S. Kandambeth, W. Zhang, J. Ming, P. T. Parvatkar, E. Abou-Hamad, O. Shekhah, L. Cavallo, M. Eddaoudi, H. N. Alshareef, *ACS Energy Lett.*. **2020**, *5*, 2256–2264.
[35] W. Wang, V. S. Kale, Z. Cao, Y. Lei, S. Kandambeth, G. Zou, Y. Zhu, E. Abouhamad, O. Shekhah, L. Cavallo, M. Eddaoudi, H. N. Alshareef, *Adv. Mater.* **2021**, *33*, e2103617.
[36] Y. Chen, J. Li, Q. Zhu, K. Fan, Y. Cao, G. Zhang, C. Zhang, Y. Gao, J. Zou, T. Zhai, C. Wang, *Angew. Chem. Int. Ed.* **2022**, *61*, e202116289.
[37] Z. Song, L. Miao, H. Duan, L. Ruhlmann, Y. Lv, D. Zhu, L. Li, L. Gan, M. Liu, *Angew. Chem. Int. Ed.* **2022**, *61*, e202208821.
[38] G. Sun, B. Yang, X. Chen, Y. Wei, G. Yin, H. Zhang, Q. Liu, *Chem. Eng. J.* **2022**, *431*, 134253.
[39] S. Zhang, S. Long, H. Li, Q. Xu, *Chem. Eng. J.* **2020**, *400*, 125898.
[40] R. Shi, L. Liu, Y. Lu, C. Wang, Y. Li, L. Li, Z. Yan, J. Chen, *Nat. Commun.* **2020**, *11*, 178.
[41] T. Lu, F. Chen, *J. Comput. Chem.* **2012**, *33*, 580–592.
[42] W. Humphrey, A. Dalke, K. Schulten, *J. Mol. Graph.* **1996**, *14*, 33–38.
[43] C. Guo, X. Huang, J. Huang, X. Tian, Y. Chen, W. Feng, J. Zhou, Q. Li, Y. Chen, S. L. Li, Y. Q. Lan, *Angew. Chem. Int. Ed.* **2024**, *63*, e202403918.
[44] Q. Zhang, P. Zhi, J. Zhang, S. Duan, X. Yao, S. Liu, Z. Sun, S. C. Jun, N. Zhao, L. Dai, L. Wang, X. Wu, Z. He, Q. Zhang, *Adv. Mater.* **2024**, *36*, e2313152.
[45] S. Zhang, J. Chen, W. Chen, Y. Su, Q. Gou, R. Yuan, Z. Wang, K. Wang, W. Zhang, X. Hu, Z. Zhang, P. Wang, F. Wan, J. Liu, B. Li, Y. Wang, G. Zheng, M. Li, J. Sun, *Angew. Chem. Int. Ed.* **2025**, *64*, e202424184.

Manuscript received: April 01, 2025
Revised manuscript received: June 23, 2025
Accepted manuscript online: July 15, 2025
Version of record online: July 29, 2025